DOI: 10.19884/j.1672-5220.202403017

Enhanced Reliability and Stability of Vanadium Oxide-Based RRAM by Constructing $VO_x/TiO_2/n^{++}$ Si p-i-n Structure

WANG Ze, ZHOU Xin, ASAD Khaleeq, WANG Chunrui*
College of Physics, Donghua University, Shanghai 201620, China

Abstract: Vanadium oxide (VO_x) has garnered significant attention in the realm of resistive random-access memory (RRAM) owing to its outstanding resistive switching characteristics. However, the ambiguous mechanisms of resistive switching and inferior stability hinder its practical applications. Herein, an RRAM named Cu/VO_x/TiO_2/n^{++} Si device is prepared. It displays bipolar resistive switching behavior and shows superior cycle endurance (>200), a significantly high on/off ratio (>10^2) and long-term stability. The tremendous improvement in the stability of the Cu/VO_x/TiO_2/n^{++} Si device compared with the Cu/VO_x/n^{++} Si device is due to the p-i-n structure of VO_x/TiO_2/n^{++} Si. The switching mechanism of the Cu/VO_x/TiO_2/n^{++} Si device is attributed to the growth and annihilation of Cu conductive filaments.

Keywords: vanadium oxide; bipolar resistive switching; p-i-n junction; resistive random-access memory (RRAM); titanium dioxide; double-layer structure
CLC number: TN386.1 **Document code**: A
Article ID: 1672-5220(2025)03-0242-09

Open Science Identity (OSID)

0 Introduction

The novel non-volatile resistive random-access memory (RRAM) boasts features of the remarkably low power consumption, high density, fast speed, facile manufacture and coherence with the complementary metal-oxide-semiconductor (CMOS) technology[1-3]. Consequently, RRAM stands as a promising frontrunner for the next epoch of memory storage technologies[4-5]. The current-voltage (*I-U*) characteristics of metal-insulator-metal (MIM) structures undergo significant change between the high-resistance state (HRS) and low-resistance state (LRS), mirroring the on and off states of logic signals[6]. Being a member of the transition metal oxides, vanadium oxide (VO_x) demonstrates outstanding resistive switching (RS) characteristics with an easily adjustable composition[7-8]. VO_x is now utilized in non-volatile memory[9-10], photoelectric detection[11] and other areas, and it holds broad research prospects. VO_x-based RRAM has made significant progress in the fabrication technology, memory performance and prospective applications[10,12]. However, a significant challenge in employing VO_x-based RRAM as a memory lies in the instability of the device within the memory states[12-13]. The instability of RS parameters in RRAM can potentially result in programming errors and misreading logic signals[14]. Reducing the instability of RS parameters has become a significant issue in RRAM. The double-layer structure can enhance the performance of manufactured devices, and it has been extensively studied, such as ZrO_x/HfO_2[14], HfO_2/TiO_2[15], MnO/CeO_2[16], MnO_x/HfO_2[17], AlO_x/HfO_x[18], TiO_2/ZnO[19], rGO/ZnO[20] and ZnO/ZrO_2[21]. Compared with single-layer RRAM, double-layer RRAM exhibits distinct advantages, such as long-term stability, significant RS performance and data retention properties[22-23]. TiO_2 is a typical wide-gap oxide semiconductor with low electrical conductivity and can be considered an intrinsic semiconductor. TiO_2 emerges as one of the most prospective candidates in RRAM due to its thermal stability and high CMOS compatibility[24-26].

In this work, we demonstrate that the Cu/VO_x/TiO_2/n^{++} Si device displays bipolar RS behavior with a superior cycle endurance (>200), a significantly high on/off ratio (>10^2), and long-term stability. The tremendous improvement in the stability of the Cu/VO_x/TiO_2/n^{++} Si device compared with the Cu/VO_x/n^{++} Si device is attributed to the p-i-n structure of VO_x/TiO_2/n^{++} Si, which effectively increases the width of the space charge region. Furthermore, we also investigate comprehensively the conductance and switching mechanism of the Cu/VO_x/TiO_2/n^{++} Si device.

1 Materials and Methods

1.1 Materials

The metals copper (purity: 99.999 5%), titanium (purity: 99.995%) and vanadium (purity: 99.9%)

Received date: 2024-03-28
Foundation item: National Natural Science Foundation of China (No. 61376017)
* Correspondence should be addressed to WANG Chunrui, email: crwang@dhu.edu.cn
Citation: WANG Z, ZHOU X, ASAD K, et al. Enhanced reliability and stability of vanadium oxide-based RRAM by constructing VO_x/TiO_2/n^{++} Si p-i-n structure[J]. *Journal of Donghua University (English Edition)*, 2025, 42(3): 242-250.

were purchased form ZhongNuo Advanced Material (Beijing) Technology Co., Ltd., China. Heavily doped n-type Si wafer (n^{++} Si) was purchased from Suzhou Crystal Silicon Electronics & Technology Co., Ltd., China.

1.2 Fabrication of $Cu/VO_x/TiO_2/n^{++}$ Si device

The schematic illustration of fabrication and characterization of the $Cu/VO_x/TiO_2/n^{++}$ Si device is depicted in Fig. 1.

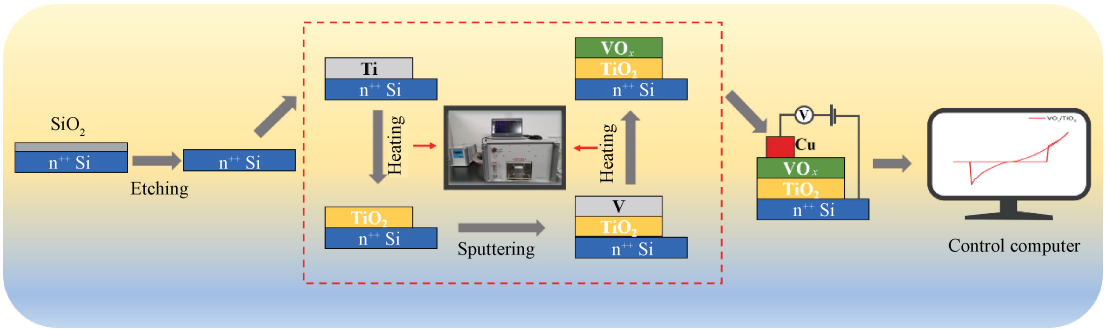

Fig. 1 Schematic illustration of fabrication and characterization of $Cu/VO_x/TiO_2/n^{++}$ Si device

Firstly, n^{++} Si was etched in hydrofluoric acid for 3 min to remove the natural silicon dioxide layer. Then the VO_x/TiO_2 double-layer structure was prepared on the etched n^{++} Si by using a sputtering-oxidation coupling method, which could be divided into four steps: sputtering of metal Ti, oxidation of metal Ti, sputtering of metal V, and oxidation of metal V. The base vacuum level in the vacuum chamber was below 1.7×10^{-3} Pa, and then the chamber was filled with Ar atmosphere to maintain the bias pressure at 1.0×10^{-1} Pa. Subsequently, Ti and V were deposited onto the n^{++} Si substrate via 144 W direct current (DC) power at room temperature with the deposition time of 8 min for Ti and 5 min for V, respectively. Before each experiment, a pre-sputtering of 5 min was conducted under the same conditions to clean the target surface.

Secondly, the obtained samples were put into rapid thermal processing (RTP) in a vacuum annealing furnace (Beijing East Star Labs, China), and oxidation was performed. The Ti film sample was oxidized at 800 ℃ for 80 s in air, and the V film sample was oxidized at 470 ℃ for 230 s. The prepared VO_x and TiO_2 were both approximately 60 nm thick, as shown in Fig. 2.

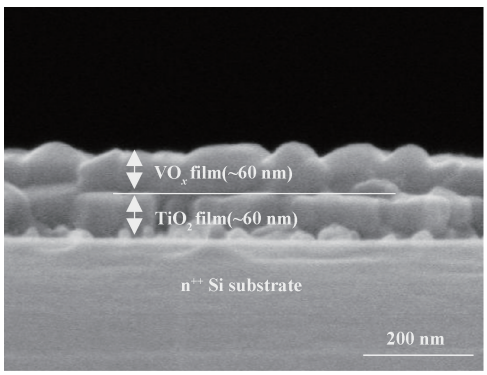

Fig. 2 Scanning electron microscopy image of double-layer structure consisting of 60 nm VO_x grown on 60 nm TiO_2 buffer layer

Finally, the $Cu/VO_x/TiO_2/n^{++}$ Si device, a circular top electrode of 600 nm in diameter, was achieved on the VO_x layer employing the DC magnetron sputtering approach, with the aid of a mask. For comparison, the $Cu/VO_x/n^{++}$ Si device was fabricated by using the same method.

1.3 Characterization of $Cu/VO_x/TiO_2/n^{++}$ Si device

A semiconductor characterization system (4200A-SCS Parameter Analyzer, Keithley, USA) on a probe station was applied to evaluate the device's *I-U* characteristics throughout testing at ambient temperature. The crystalline structures of thin films were recorded by employing X-ray diffraction (XRD) (Rigaku, $\lambda=1.54056$ Å, Japan). X-ray photoelectron spectroscopy (XPS) data of the VO_x thin films and TiO_2 thin films were obtained by a spectrometer (Escalab 250Xi, Thermo Scientific, USA) with an excitation source of Al Kα radiation.

2 Results and Discussion

2.1 Bipolar RS characteristics

The *I-U* characteristics of the $Cu/VO_x/TiO_2/n^{++}$ Si device were measured using a −3 V to 3 V round-trip voltage sweep. As depicted in Fig. 3(a), the device exhibits typical bipolar RS behavior. Notably, the current undergoes a sharp increase at a certain voltage during the sweep from 0 V to 3 V, indicating that the device is "set"[27] from HRS to LRS. Subsequently, the voltage sweeps back from 3 V to 0 V, and the LRS is maintained. Conversely, when the reverse bias sweeps from 0 V to −3 V, a similar sharp decrease in current at a certain voltage indicates that the device is "reset"[28-29] from LRS to HRS. Upon returning from −3 V to 0 V, the HRS is sustained. Remarkably, the RS characteristics remain consistent over 100 switching cycles, mirroring those of the initial sweep, as depicted in Fig. 3(b). The cycle endurance of the $Cu/VO_x/TiO_2/n^{++}$ Si device demonstrates high reliability (on/off

ratio $>10^2$) and superior cycle endurance (>200) (Fig. 3(c)), which is superior to that of the Cu/VO_x/n^{++} Si device (Fig. 4(a)). Specifically, the resistance in LRS measures around 10^3 Ω and the resistance of HRS exceeds 10^5 Ω. However, the on/off ratio exhibits sweep-cycle-number-dependent degradation. Cu^{2+} is usually concentrated in some local areas in HRS, while it redistributes in LRS. After multiple formation and annihilation processes of Cu filaments, Cu^{2+} may gradually redistribute in HRS. The redistribution leads to excessive diffusion and a resistance decrease in LRS and HRS. At a voltage of 0.5 V, the Cu/VO_x/TiO_2/n^{++} Si device shows narrower dispersion in HRS and LRS cumulative distributions compared to the Cu/VO_x/n^{++} Si device (Fig. 3(d)). The RS performance of the Cu/VO_x/TiO_2/n^{++} Si device is notably enhanced compared to the Cu/VO_x/n^{++} Si device. Concurrently, the power consumption is reduced owing to the comparatively elevated resistance of the Cu/VO_x/TiO_2/n^{++} Si device in HRS and LRS, thereby contributing to enhanced stability.

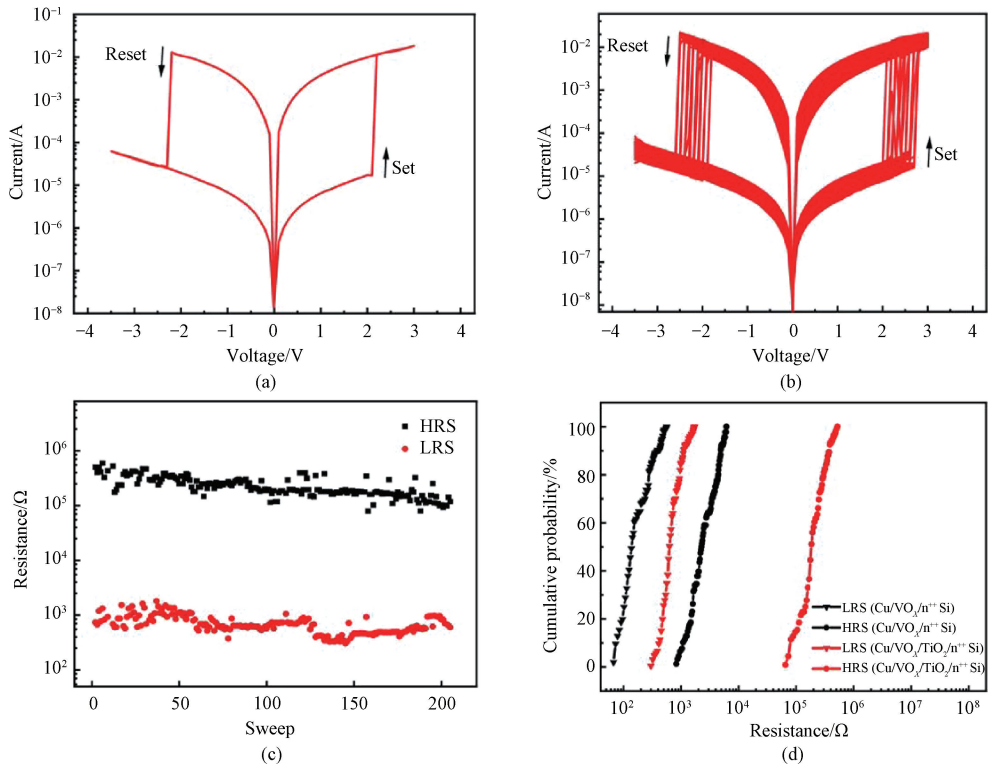

Fig. 3 Performance of Cu/VO_x/TiO_2/n^{++} Si device: (a) typical bipolar DC *I-U* curve; (b) *I-U* curves in 100 cycles; (c) cycle endurance at 0.5 V; (d) comparison of cumulative distribution in HRS and LRS for Cu/VO_x/TiO_2/n^{++} Si device and Cu/VO_x/n^{++} Si device

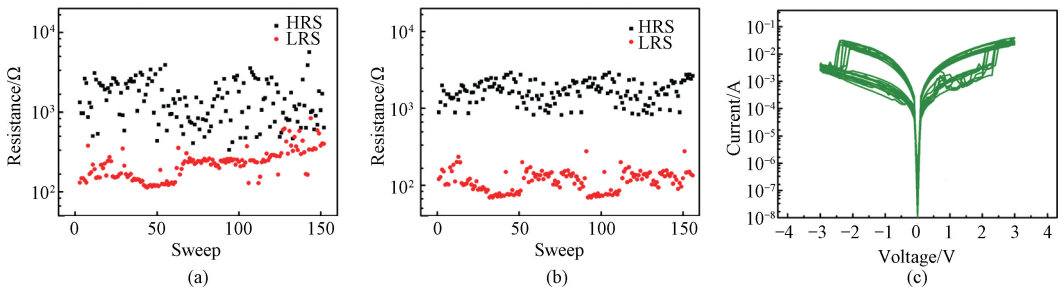

Fig. 4 Performance of Cu/VO_x/n^{++} Si device: (a) cycle endurance at 0.5 V; (b) cycle endurance at −0.5 V; (c) typical bipolar DC *I-U* curve

2.2 p-i-n junction effects and RS mechanism

To deeply investigate the switching mechanism of the $Cu/VO_x/TiO_2/n^{++}$ Si device, we fabricated and characterized the VO_x thin film field effect transistor (FET) with metal contacts serving as source/drain electrodes and a silicon substrate as the back gate. Figure 5(a) shows the output characteristics (I_{DS}-U_{DS}) at various back-gate voltages of VO_x FET, where U_{DS} denotes the drain-source voltage, I_{DS} denotes the drain-source current, and U_G denotes the back-gate voltage. Figure 5(b) depicts the transfer characteristics at three different U_{DS} of VO_x thin film FET, clearly indicating a pronounced p-type electrical conduction behavior[30], thereby demonstrating the p-type semiconductor properties of VO_x.

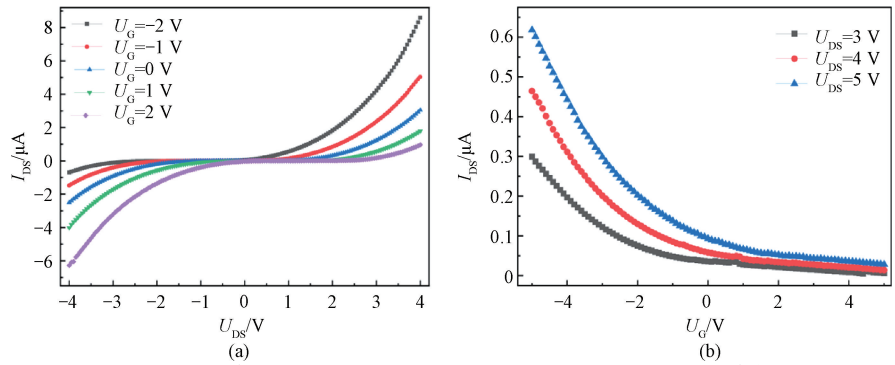

Fig. 5 VO_x thin film FET testing: (a) output characteristics at different back-gate voltages; (b) transfer characteristics at different drain-source voltages

The VO_x/n^{++} Si structure forms a p-n junction[31], with its energy band diagram illustrated in Fig. 6, where E_c represents the conduction band edge, E_v denotes the valence band edge, and W_d indicates the width of the space charge region. Upon the application of a positive bias U_+ to the top electrode of Cu, the p-n junction undergoes forward bias (Fig. 6(b)). The external electric field reduces the width of the space charge region and lowers the interface barrier, promoting diffusion current through the junction. The decrease in the width of the space charge region may lead to a greater acceleration of electrons, increasing the possibility of electrons crossing the energy barrier. If the electric field strength is too high, a breakdown may occur. This explains why instability in the cycle endurance of the $Cu/VO_x/n^{++}$ Si device at 0.5 V is discerned in HRS (Fig. 4(a)), leading to a conspicuous uneven distribution. Conversely, applying a negative bias U_- to the n^{++} Si bottom electrode reverse-biases the p-n junction (Fig. 6(c)), expanding the space charge region width and elevating the barrier under the external electric field. This curtails the diffusion current through the junction, significantly improving the uneven resistance distribution in HRS (Fig. 4(b) and Fig. 4(c)).

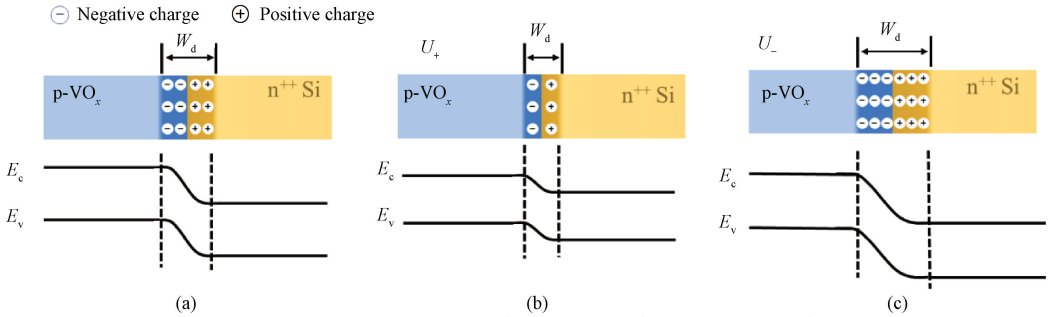

Fig. 6 Energy band diagram of p-n junction: (a) zero bias; (b) positive bias; (c) negative bias

To eliminate the uneven resistance distribution in HRS, we introduced rutile phase TiO_2 (TiO_2(R)) as a buffer layer to form the $Cu/VO_x/TiO_2/n^{++}$ Si device. XRD pattern of TiO_2(R) is shown in Fig. 7. At room temperature, TiO_2 is a typical wide-gap oxide semiconductor with low electrical conductivity and can be considered an intrinsic semiconductor[32], so the $VO_x/TiO_2/n^{++}$ Si structure is regarded as the p-i-n junction. The p-i-n structure effectively increases the width of the space charge region and tremendously improves the reliability and stability of the $VO_x/TiO_2/n^{++}$ Si device.

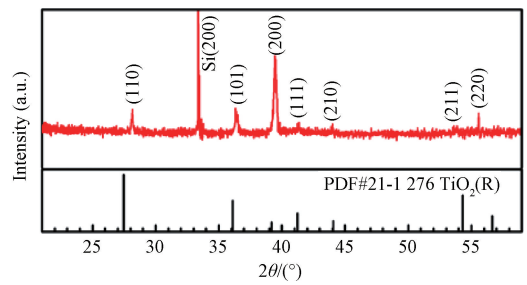

Fig. 7 XRD patterns of TiO_2(R) thin film

The X-ray photoelectron spectroscopy (XPS) spectrum of the V 2p area was analyzed to study the RS mechanism in the $Cu/VO_x/TiO_2/n^{++}$ Si device, as illustrated in Fig. 8(a). All values were aligned with respect to C 1s. To minimize the binding energy gap across O 1s and V 2p core levels, the tailoring technique required a simultaneous analysis of the entire spectrum range for both core levels. XPS probed on VO_x grown on a silicon substrate revealed a set of binding energies at 517.8 eV and 516.5 eV, which were indicative of V^{5+} and V^{4+} within the $V\ 2p_{3/2}$ peak, respectively[33]. The positions of O 1s peaks, corresponding to the oxide, O—Si bonds and H_2O species, are fixed at 530.0, 532.3 and 533.6 eV, respectively[33]. The relative concentrations of V^{5+} and V^{4+} are quantified as 90.4% and 9.6%, respectively, through XPS peak area integration. According to XPS results, the x value of approximately 2.45 in VO_x suggests V_2O_5 is the main component of the VO_x dielectric layer, with little VO_2 content[34]. Therefore, the RS mechanism of the device is not related to the threshold of VO_2[35-36], but rather to the RS of V_2O_5[34,37]. Besides, the content of high-valence vanadium is dominant, indicating the presence of a small number of oxygen vacancies[38], which is consistent with the results of XRD, as shown in Fig. 9, further demonstrating that the p-type VO_x is attributed to a relatively low internal concentration of oxygen vacancies.

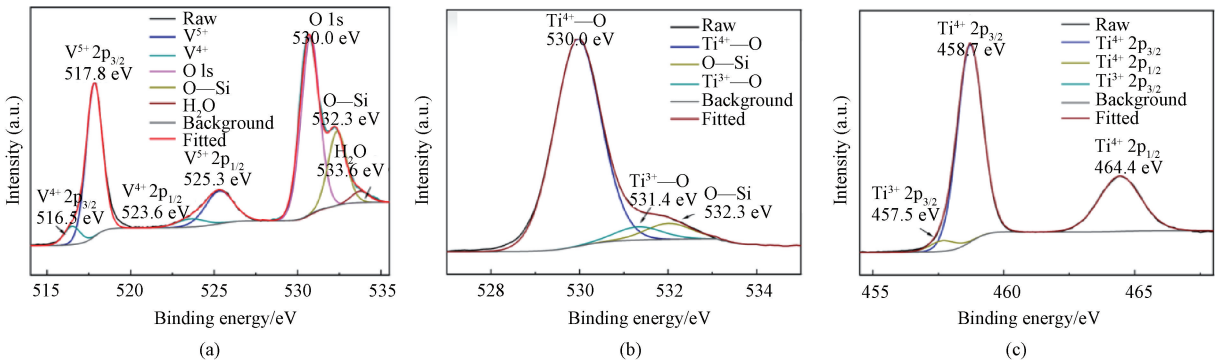

Fig. 8 XPS narrow scan spectra: (a) V 2p and O 1s spectra of VO_x thin films; (b) O 1s spectra of TiO_2 thin films; (c) Ti 2p spectra of TiO_2 thin films

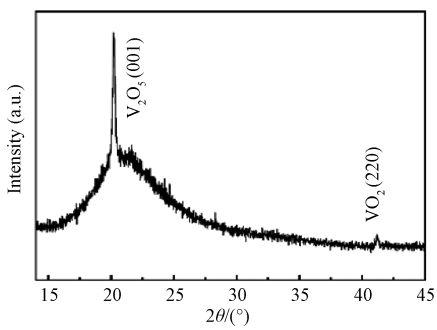

Fig. 9 XRD pattern of VO_x thin film

In the realm of oxide-based RRAM, the RS mechanism can be ascribed to either metal conductive filaments (CFs)[39-40] or oxygen vacancies[15]. To delve into this inquiry, we scrutinized the XPS spectra of O 1s and Ti 2p of TiO_2, as depicted in Figs. 8(b) and 8(c), respectively. In Fig. 8(b), the main peak at 530.0 eV corresponds to the Ti^{4+}—O bonds within the TiO_2 lattice[41]. The shoulder peak at 532.3 eV corresponds to the O—Si bonds[42]. The shoulder peak at 531.4 eV corresponds to the Ti^{3+}—O bonds, indicating the minor concentration of oxygen vacancies[43]. Meanwhile, the binding energy of Ti 2p appears as a sharp peak in Fig. 8(c). The peaks at 458.7 eV and 464.4 eV correspond to the Ti^{4+} $2p_{3/2}$ and Ti^{4+} $2p_{1/2}$ orbitals, respectively[44]. The low shoulder peak at 457.5 eV corresponds to the Ti^{3+} $2p_{3/2}$ orbital, and the shoulder peak of the Ti^{3+} $2p_{1/2}$ orbital was not found, confirming the low concentration of oxygen vacancies in TiO_2[43]. Furthermore, the XPS spectrum analysis of VO_x also reveals the presence of a small number of oxygen vacancies[38]. Consequently, the RS mechanism of the double-layer $Cu/VO_x/TiO_2/n^{++}$ Si device is primarily ascribed to the presence of Cu CFs.

Figure 10 illustrates the RS process facilitated by Cu CFs in the $Cu/VO_x/TiO_2/n^{++}$ Si device. When a positive bias is applied to the top electrode of Cu in Fig. 10(a), Cu atoms oxidize into Cu^{2+} ions ($Cu-2e^- \rightarrow Cu^{2+}$), and Cu^{2+} ions eventually migrate to the bottom electrode of n^{++} Si. Subsequently, Cu^{2+} ions undergo reduction, transforming back into Cu atoms ($Cu^{2+}+2e^- \rightarrow Cu$), and forming Cu CFs. These Cu CFs establish a connection between the bottom electrode of n^{++} Si and the top electrode of Cu, resulting in the device switching to LRS as depicted in Fig. 10(b). Conversely, under a negative bias, the Cu atoms near the n^{++} Si electrode are oxidized into Cu^{2+} ions, and then they migrate towards the top electrode of Cu. Meanwhile, the annihilation of Cu CFs causes it to disconnect, and the RRAM device turns to HRS as depicted in Fig. 10(c).

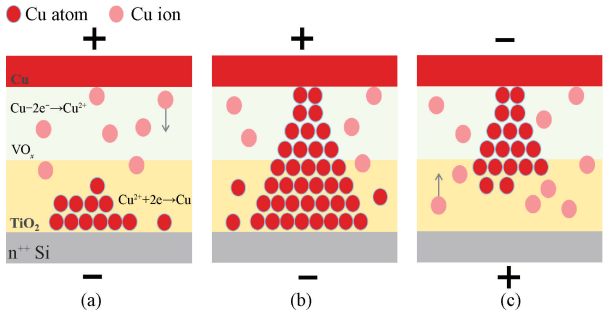

Fig. 10 Schematic diagram of RS process: (a) redox reaction occurring at the positive and negative contact surfaces (positive bias); (b) Cu conductive filaments (positive bias); (c) fractured Cu conductive filaments (negative bias)

To clarify the RS mechanism of the $Cu/VO_x/TiO_2/n^{++}$ Si device, the current conduction mechanism in HRS and LRS was analyzed. The RS mechanism is ascribed to the process of Cu CFs growth and annihilation[45-46]. In Fig. 11(a), the linear fitting of $\lg I$-$\lg U$ in LRS under positive bias is presented. The slope of $\lg I$ vs. $\lg U$ is around 1.2, indicating a nearly linear correlation and suggesting that the current conduction mechanism in LRS can be ascribed to Ohmic conduction[47-48]. As depicted in Fig. 11(b), the fitting result in HRS reveals a linear correlation between $\lg I$ and $U^{0.5}$, implying that the current conduction mechanism is employed by Schottky emission control[49]. Based on these aforementioned conduction mechanisms, we propose a switching model for the $Cu/VO_x/TiO_2/n^{++}$ Si device. In HRS, the current conduction mechanism is impeded by the Schottky emission, and electrons surpass the potential energy barrier between the switching layer and the electrode. Conversely, in LRS, the current conduction mechanism is facilitated by the presence of Cu CFs. By applying a positive bias to the top electrode of Cu, a continuous formation of Cu CFs drives the RRAM device from HRS to LRS. During the reset process, the oxidation of Cu leads to the rupture of Cu CFs, prompting the device to switch back to HRS.

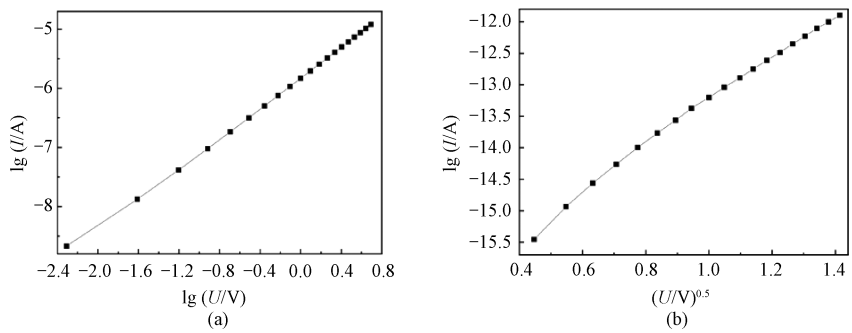

Fig. 11 Analysis of current conduction mechanism: (a) $\lg I$-$\lg U$ curve of $Cu/VO_x/TiO_2/n^{++}$ Si device in LRS; (b) $\lg I$-$U^{0.5}$ curve of $Cu/VO_x/TiO_2/n^{++}$ Si device in HRS

2.3 Retention performance analysis

In our study on the stability of the $Cu/VO_x/TiO_2/n^{++}$ Si device, we present the retention yield of the device fabricated at room temperature, as depicted in Fig. 12. The HRS and LRS were assessed utilizing a read voltage of 0.5 V over a retention duration of 4 500 s. The substantial retention properties, ensuring a high resistance ratio, are pivotal for the preservation of stored data. Our work underscores the enhanced attributes of the $Cu/VO_x/TiO_2/n^{++}$ Si device, including superior cycle endurance, a significantly high on/off ratio and long-term stability. These findings not only validate the potential of the $Cu/VO_x/TiO_2/n^{++}$ Si device but also highlight its promising prospects for applications in the RRAM technology.

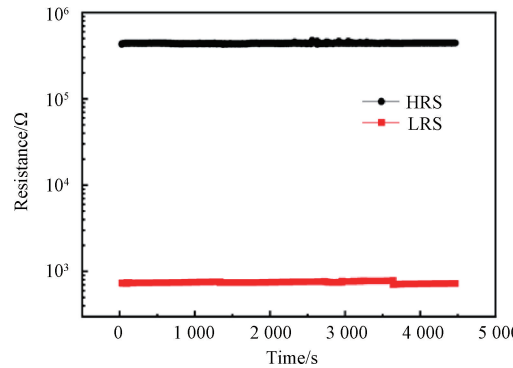

Fig. 12 Retention properties of $Cu/VO_x/TiO_2/n^{++}$ Si device at 0.5 V

3 Conclusions

In summary, the double-layer Cu/VO_x/TiO_2/n^{++} Si RRAM exhibits excellent performance. This is attributed to the p-i-n structure of VO_x/TiO_2/n^{++} Si, which effectively increases the width of the space charge region and results in tremendous improvement of reliability and stability. The bipolar RS behavior can be ascribed to the dynamic processes of growth and annihilation of Cu CFs occurring within the oxide layer.

References

[1] PRAKASH A, PARK J, SONG J, et al. Demonstration of low power 3-bit multilevel cell characteristics in a TaO_x-based RRAM by stack engineering[J]. *IEEE Electron Device Letters*, 2015, 36(1): 32-34.

[2] PUGLISI F M, QAFA A, PAVAN P. Temperature impact on the reset operation in HfO_2 RRAM[J]. *IEEE Electron Device Letters*, 2015, 36(3): 244-246.

[3] WANG G M, LONG S B, YU Z A, et al. Improving resistance uniformity and endurance of resistive switching memory by accurately controlling the stress time of pulse program operation[J]. *Applied Physics Letters*, 2015, 106(9): 092103.

[4] YANG M K, KIM G H, JU H, et al. The interfacial layer effect on bi-stable resistive switching phenomenon in MnO_x thin film[J]. *Applied Physics Letters*, 2015, 107(5): 053503.

[5] MAESTRO M, MARTIN-MARTINEZ J, DIAZ J, et al. Analysis of set and reset mechanisms in Ni/HfO_2-based RRAM with fast ramped voltages [J]. *Microelectronic Engineering*, 2015, 147: 176-179.

[6] LANZA M. A review on resistive switching in high-k dielectrics: a nanoscale point of view using conductive atomic force microscope[J]. *Materials*, 2014, 7(3): 2155-2182.

[7] FU Y Y, ZHOU Y, HUANG X D, et al. Reconfigurable synaptic and neuronal functions in a V/VO_x/$HfWO_x$/Pt memristor for nonpolar spiking convolutional neural network [J]. *Advanced Functional Materials*, 2022, 32(23): 2270130.

[8] IQBAL S, DUY L T, KANG H, et al. Femtojoule-power-consuming synaptic memtransistor based on mott transition of multiphasic vanadium oxides [J]. *Advanced Functional Materials*, 2021, 31(46): 2102567.

[9] IVANOV A I, GUTAKOVSKII A K, KOTIN I A, et al. Resistive switching effect with ON/OFF current relation up to 10^9 in 2D printed composite films of fluorinated graphene with V_2O_5 nanoparticles [J]. *Advanced Electronic Materials*, 2019, 5(10): 1900310.

[10] CHEN K H, LIAO C H, TSAI J H, et al. Electrical conduction and bipolar switching properties in transparent vanadium oxide resistive random access memory (RRAM) devices[J]. *Applied Physics A*, 2013, 110(1): 211-216.

[11] PAWAR M S, BANKAR P K, MORE M A, et al. Ultra-thin V_2O_5 nanosheet based humidity sensor, photodetector and its enhanced field emission properties[J]. *RSC Advances*, 2015, 5 (108): 88796-88804.

[12] LI J P, ZHOU X, XU L, et al. Bipolar resistive switching in Ag/VO_2 (B)/SiO_x/n^{++} Si RRAM [J]. *Materials Research Express*, 2022, 9(3): 035003.

[13] WONG F J, SRIRAM T S, SMITH B R, et al. Bipolar resistive switching in room temperature grown disordered vanadium oxide thin-film devices[J]. *Solid-State Electronics*, 2013, 87: 21-26.

[14] LEE J, BOURIM E M, LEE W, et al. Effect of ZrO_x/HfO_x bilayer structure on switching uniformity and reliability in nonvolatile memory applications[J]. *Applied Physics Letters*, 2010, 97(17): 172105.

[15] YE C, DENG T F, ZHANG J C, et al. Enhanced resistive switching performance for bilayer HfO_2/TiO_2 resistive random access memory [J]. *Semiconductor Science and Technology*, 2016, 31(10): 105005.

[16] HU Q L, KANG T S, ABBAS H, et al. Resistive switching characteristics of Ag/MnO/CeO_2/Pt heterostructures memory devices[J]. *Microelectronic Engineering*, 2018, 189: 28-32.

[17] HU Q L, ABBAS H, KANG T S, et al. Forming-free resistive switching characteristics in manganese oxide and hafnium oxide devices[J]. *Japanese Journal of Applied Physics*, 2019, 58 (4): 044001.

[18] QI M, FU T Q, YANG H D, et al. Reliable analog resistive switching behaviors achieved using memristive devices in AlO_x/HfO_x bilayer structure for neuromorphic systems [J]. *Semiconductor Science and Technology*, 2022, 37 (3): 035018.

[19] JAIN P K, SALIM M, CHAND U, et al. Switching characteristics in TiO_2/ZnO double layer resistive switching memory device [J]. *Materials Research Express*, 2017, 4 (6): 065901.

[20] LIN C L, CHANG W Y, HUANG Y L, et al. Resistance switching behavior of ZnO resistive random access memory with a reduced graphene oxide capping layer [J]. *Japanese Journal of*

Applied Physics, 2015, 54(4S): 04DJ08.
[21] JIAN W Y, YOU H C, WU C Y. Resistive switching mechanism of ZnO/ZrO_2-stacked resistive random access memory device annealed at 300 ℃ by sol-gel method with forming-free operation [J]. *Japanese Journal of Applied Physics*, 2018, 57(1): 011501.
[22] LEE H Y, CHEN P S, WU T Y, et al. Low power and high speed bipolar switching with a thin reactive Ti buffer layer in robust HfO_2 based RRAM [C]//2008 IEEE International Electron Devices Meeting, San Francisco, CA, USA. New York: IEEE, 2008: 1-4.
[23] ZHOU G D, XIAO L H, ZHANG S J, et al. Mechanism for an enhanced resistive switching effect of bilayer NiO_x/TiO_2 for resistive random access memory [J]. *Journal of Alloys and Compounds*, 2017, 722: 753-759.
[24] CHOI J, KIM S. Improved stability and controllability in ZrN-based resistive memory device by inserting TiO_2 layer [J]. *Micromachines*, 2020, 11(10): 905.
[25] HSIUNG C P, LIAO H W, GAN J Y, et al. Formation and instability of silver nanofilament in Ag-based programmable metallization cells [J]. *ACS Nano*, 2010, 4(9): 5414-5420.
[26] DAI Y W, BAO W Z, HU L F, et al. Forming free and ultralow-power erase operation in atomically crystal TiO_2 resistive switching [J]. *2D Materials*, 2017, 4(2): 025012.
[27] REHMAN M M, REHMAN H M M U, GUL J Z, et al. Decade of 2D-materials-based RRAM devices: a review [J]. *Science and Technology of Advanced Materials*, 2020, 21(1): 147-186.
[28] HANSEN M, ZIEGLER M, KOLBERG L, et al. A double barrier memristive device [J]. *Scientific Reports*, 2015, 5: 13753.
[29] HAZRA P, JINESH K B. Vertical limits of resistive memory scaling: the detrimental influence of interface states [J]. *Applied Physics Letters*, 2020, 116(17): 173502.
[30] WANG C, WANG C R, SUN L, et al. Synthesis and characteristics of p-type CdS nanobelts [J]. *Materials Research Express*, 2017, 4(11): 115013.
[31] SPROUL A. Understanding the p-n junction [M]//LARGENT R, WENHAM S. Solar cells resources for the secondary science teacher. Sydney: UNSW, 2003: 13-24.
[32] NOSAKA Y, NOSAKA A Y. Reconsideration of intrinsic band alignments within anatase and rutile TiO_2 [J]. *The Journal of Physical Chemistry Letters*, 2016, 7(3): 431-434.
[33] BONDARENKA V, GREBINSKIJ S, MICKEVIČIUS S, et al. Determination of vanadium valence in hydrated compounds [J]. *Journal of Alloys and Compounds*, 2004, 382(1/2): 239-243.
[34] HOTA M K, NAGARAJU D H, HEDHILI M N, et al. Electroforming free resistive switching memory in two-dimensional VO_x nanosheets [J]. *Applied Physics Letters*, 2015, 107(16): 163106.
[35] ZHOU X, ZHAO L, ZHEN W L, et al. Phase-transition-induced VO_2 thin film IR photodetector and threshold switching selector for optical neural network applications [J]. *Advanced Electronic Materials*, 2021, 7(5): 2001254.
[36] ZHANG K L, WANG B L, WANG F, et al. VO_2-based selection device for passive resistive random access memory application [J]. *IEEE Electron Device Letters*, 2016, 37(8): 978-981.
[37] IVANOV A I, PRINZ V Y, ANTONOVA I V, et al. Resistive switching on individual V_2O_5 nanoparticles encapsulated in fluorinated graphene films [J]. *Physical Chemistry Chemical Physics*, 2021, 23(36): 20434-20443.
[38] ZHAN Y J, LU Y, XIAO X D, et al. Tuning thermochromic performance of VO_x-based multilayer films by controlling annealing pressure [J]. *Ceramics International*, 2020, 46(2): 2079-2085.
[39] SUN K, ZHANG K L, WANG F, et al. An increasing high resistance state phenomenon in $Al/VO_x/Cu$ resistive switching device [J]. *ECS Transactions*, 2014, 60(1): 1057-1062.
[40] ZHANG H Z, ZHANG K L, WANG F, et al. Effect of VO_x interlayer in $Cu/HfO_x/TiN$ cell and its resistive switching mechanism [C]//2015 China Semiconductor Technology International Conference, Shanghai, China. New York: IEEE, 2015: 1-3.
[41] PANDA A B, MAHAPATRA S K, BARHAI P K, et al. Understanding of gas phase deposition of reactive magnetron sputtered TiO_2 thin films and its correlation with bactericidal efficiency [J]. *Applied Surface Science*, 2012, 258(24): 9824-9831.
[42] JEONG H Y, LEE J Y, CHOI S Y. Interface-engineered amorphous TiO_2-based resistive memory devices [J]. *Advanced Functional Materials*, 2010, 20(22): 3912-3917.
[43] ZHANG R L, HUANG H, XIA Q, et al. Role of oxygen vacancies at the TiO_2/HfO_2 interface in flexible oxide-based resistive switching memory [J]. *Advanced Electronic Materials*, 2019, 5(5): 1800833.
[44] SAMPATH S, MAYDANNIK P, IVANOVA T, et al. Efficient solar photocatalytic activity of TiO_2 coated nano-porous silicon by atomic layer deposition [J]. *Superlattices and Microstructures*, 2016, 97: 155-166.

[45] SAWA A. Resistive switching in transition metal oxides[J]. *Materials Today*, 2008, 11(6): 28-36.
[46] KWON D H, KIM K M, JANG J H, et al. Atomic structure of conducting nanofilaments in TiO_2 resistive switching memory [J]. *Nature Nanotechnology*, 2010, 5(2): 148-153.
[47] SUN Y M, SONG C, YIN J, et al. Guiding the growth of a conductive filament by nanoindentation to improve resistive switching [J]. *ACS Applied Materials & Interfaces*, 2017, 9(39): 34064-34070.
[48] SUN Y M, SONG C, YIN J, et al. Modulating metallic conductive filaments via bilayer oxides in resistive switching memory[J]. *Applied Physics Letters*, 2019, 114(19): 193502.
[49] SIMMONS J G. Poole-Frenkel effect and Schottky effect in metal-insulator-metal systems [J]. *Physical Review*, 1967, 155(3): 657-660.

构建 $VO_x/TiO_2/n^{++}$ Si 的 p-i-n 结构提高钒氧化物基阻变存储器的可靠性和稳定性

王 泽, 周 鑫, ASAD Khaleeq, 王春瑞*
东华大学 物理学院, 上海 201620

摘 要: 氧化钒（VO_x）由于其出色的电阻开关特性，在阻变存储器（resistive random-access memory, RRAM）领域受到广泛关注。然而，模糊的电阻开关机理和较差的稳定性阻碍了其实际应用。该文制备了名为 Cu/VO_x/TiO_2/n^{++} Si 的阻变存储器。该阻变存储器具有双极性电阻开关特性，表现出卓越的循环耐久性(>200)，显著的高开/关比（$>10^2$）和长期稳定性。$VO_x/TiO_2/n^{++}$ Si 的 p-i-n 结构使 Cu/VO_x/TiO_2/n^{++} Si 器件的稳定性比 Cu/VO_x/n^{++} Si 器件高。该阻变存储器的开关机制源于铜导电细丝的生长和湮没。

关键词: 氧化钒；双极电阻开关；p-i-n 结；阻变存储器；二氧化钛；双层结构